



Enhanced catalytic degradation of methylene blue by α -Fe₂O₃/graphene oxide via heterogeneous photo-Fenton reactions

Yuyang Liu^a, Wei Jin^b, Yaping Zhao^{a,*}, Guangshan Zhang^c, Wen Zhang^{d,*}

^a School of Ecological and Environmental Science, Shanghai Key Laboratory for Urban Ecological Process and Eco-Restoration, East China Normal University, Shanghai 200241, China

^b School of Environmental Science and Engineering, Tongji University, Shanghai 200071, China

^c School of Municipal and Environmental Engineering, Harbin Institute of Technology, Harbin 150090, China

^d John A. Reif, Jr. Department of Civil and Environmental Engineering, New Jersey Institute of Technology, Newark, NJ 07102, United States

ARTICLE INFO

Article history:

Received 2 September 2016

Received in revised form 23 January 2017

Accepted 27 January 2017

Available online 30 January 2017

Keywords:

Heterogeneous Fenton reaction

Dye wastewater

Hematite

Graphene oxide

Organic structures

ABSTRACT

Novel hybrid nanostructures or nanocomposites are receiving increasing attention due to their newly evolved properties. In this work, α -Fe₂O₃ anchored to graphene oxide (GO) nanosheet (α -Fe₂O₃@GO) was synthesized through a facile hydrolysis process and its photo-catalytic performances and durability in heterogeneous Fenton system were fully evaluated. The decolorization rates of methylene blue in α -Fe₂O₃@GO + H₂O₂ + UV system within a wide pH range were approximately 2.9-fold that of classical Degussa P25 TiO₂ + UV and 2.4-fold that of α -Fe₂O₃ + H₂O₂ + UV. This enhanced decolorization of methylene blue (MB) in α -Fe₂O₃@GO + H₂O₂ + UV system were attributed to the unique incorporation of GO into the catalyst which not only mediated the morphology of active sites α -Fe₂O₃ nanoparticles but also offered high electron conductivity and electrostatic attraction between negatively charged GO with positively charged MB. High efficiencies of degradation were achieved on various surface charged organic pollutants (around 96–100%), such as cationic compounds of MB and rhodamine B (RhB), anionic compound Orange II (OII) and Orange G (OG), neutral compounds of phenol, 2-nitrophenol (2-NP) and endocrine disrupting compound 17 β -estradiol (E2). The dominant reactive oxygen species (ROS) responsible for decolorization, such as hydroxyl radicals (\bullet OH) and superoxide anion radicals ($O_2^{\bullet-}$) generated by activation of H₂O₂ on the surface of α -Fe₂O₃@GO were detected and quantified by free radical quenching methods. The possible degradation mechanism of MB involved the rupture of phenothiazine ring by desulfurization and the rupture of phenyl ring due to the attack of ROS, which was analyzed by LC/MS/MS. The reduction of MB and its intermediates was consistent with the decreasing trend of the acute toxicity towards luminous bacteria with the increasing irradiation time. The results lay a foundation for highly effective and durable photo-Fenton technologies for organic wastewater within wider pH ranges than the conventional photo-Fenton reaction.

© 2017 Elsevier B.V. All rights reserved.

1. Introduction

Dye wastewater pollution has been a critical issue in recent years owing to the massive production and applications. For instance, more than 100,000 commercially available dyes are produced at an estimated annual rate of over 7×10^5 tons globally [1]. Industries, including textile, food, paper, printing, leather and cosmetic, are the main sources of dye wastewater [2]. Because of their toxicity and potentially carcinogenic nature, dyes pose

serious threat to the human health and the environment [3]. Therefore, it is important to remove these dye pollutants from wastewater effluents using efficient processes [4,5].

As one of the important advanced oxidation processes (AOPs), the conventional homogeneous Fenton process holds great promise in the treatment of the refractory organic compounds due to power of generating highly reactive hydroxyl radicals (\bullet OH) by activating H₂O₂ with Fe²⁺ [6–8]. However, the major drawbacks that limit the practical applications of the traditional Fenton process include: (i) a narrow working pH range (pH < 3); (ii) high iron concentrations in the final effluent that requires costly removal treatment and generate iron-containing sludge; and (iii) a high demand for H₂O₂ [9]. To overcome these drawbacks, heterogeneous Fenton processes have emerged as promising alternatives because of their high efficient

* Corresponding authors.

E-mail addresses: ypzhao@des.ecnu.edu.cn (Y. Zhao), wzhang81@njit.edu (W. Zhang).

activity, wide application pHs and durability [10]. Nevertheless, heterogeneous iron oxide Fenton catalysts (e.g., Fe_3O_4 [11], $\alpha\text{-Fe}_2\text{O}_3$ [12], $\gamma\text{-Fe}_2\text{O}_3$ [13], $\alpha\text{-FeOOH}$ [14,15], $\beta\text{-FeOOH}$ [16,17], and $\gamma\text{-FeOOH}$ [18]) usually have lower activities in decomposing H_2O_2 than their homogeneous counterparts do, because of the potential diffusion resistance for reactants enter the surface of the catalysts. Moreover, some catalysts have poor durability or stability due to metal leaching in oxidation conditions [19]. Therefore, developing effective and durable catalysts remains a challenge.

To date, nanostructured iron oxides have been widely used as heterogeneous Fenton catalysts, primarily because of their abundance, environmental benign, and the effective generation of surface iron complex and hydroxyl radicals under UV irradiation [20]. Among them, $\alpha\text{-Fe}_2\text{O}_3$ is the most common crystalline polymorph of Fe_2O_3 and an n-type semiconductor with small band gap of approximately 2.2 eV that can absorb light with a wavelength up to 560 nm and capable for oxide organic substrates. Besides, $\alpha\text{-Fe}_2\text{O}_3$ is more chemically and thermally stable with low iron release or dissolution when used as a heterogeneous Fenton catalyst in diverse fields [21]. Unfortunately, the reaction activity of $\alpha\text{-Fe}_2\text{O}_3$ in Fenton system is usually lower than that of $\gamma\text{-Fe}_2\text{O}_3$, $\gamma\text{-FeOOH}$, $\alpha\text{-FeOOH}$ and Fe_3O_4 due to the high electron-hole recombination rate [21,22]. Practical applications of $\alpha\text{-Fe}_2\text{O}_3$ have also been hampered by aggregation. To improve the photochemical and catalytic properties, different supports were hybridized with $\alpha\text{-Fe}_2\text{O}_3$, such as activated carbon [23], alginate [24], clay [25], bentonite [26], kaolin [27], zeolite [28], and CNTs [29]. Comparing with aforementioned supports, Graphene would endow $\alpha\text{-Fe}_2\text{O}_3$ more improved catalytic activity due to its two dimensional (2D) carbonaceous mono-layered structure, excellent thermal conductivity, electronic properties and high surface area (e.g. 2600 m^2/g) [30,31]. The multiple oxygen-containing functional groups (carboxyl, hydroxyl, and epoxy) covalently attach to its layers, resulting in a negatively charged surface [32]. The oxygen functional groups on graphene oxide sheet serve as activation sites for nucleation and growth of iron precursors to form graphene supported metal oxide-containing nanocomposites [33,34] aiming to fabricate $\alpha\text{-Fe}_2\text{O}_3$ @graphene composites with unique properties and applications [35,36]. So far, $\alpha\text{-Fe}_2\text{O}_3$ @graphene nanocomposites in many past studies are primarily used as anode materials for lithium-ion batteries [37], advanced energy storage devices [38], supercapacity [39], and electrochemical sensor [40,41]. Only a few studies reported the catalytic applications in the treatment of dye pollutants [42]. The previously reported synthesis methods often involved the use of toxic organic chemicals (e.g., hydrazine), high temperatures or high pressures, which may reduce the scalability and cost effectiveness of the applications. For example, Qiu et al. reported that Fe_2O_3 nanocrystals were in situ grown on the surface of graphene aerogels by a Stober-like method using ethanol and acetonitrile as cosolvents at a high temperature and a high pressure [43]. Xu et al. reported the fabrication of Fe_2O_3 @Graphene microsphere through a two-step spray-drying process under 150–280 °C [41]. Zhang et al. used GO, FeCl_2 , and urea to synthesize Fe_2O_3 @graphene under microwave heater with N_2 protection [44]. Wang et al. synthesized Fe_2O_3 @graphene by coating ferric on graphene oxide and then reduced via H_2 within 12 h [45]. Zhu et al. reported that Fe_2O_3 @graphene was synthesized involved the precipitation of ferric with urea and then regeneration of GO by hydrazine [46]. Additionally, there is a lack of detailed investigations on the mechanisms of the enhanced degradation efficiency or pathways of dye pollutants [41]. For example, the enhanced heterogeneous Fenton degradation of MB was investigated by nanoscale zero valent iron (nZVI) assembled on magnetic Fe_3O_4 /reduced graphene oxide ($\text{Fe-Fe}_3\text{O}_4$ @rGO) [33]. In this study, the optimum operation pH was 3, above which the decolorization ratio of MB sharply decreased. Therefore, this new catalyst

was actually able to overcome the drawbacks of homogeneous Fenton reaction. Also, the decolorization ratio of MB catalyzed by $\text{Fe-Fe}_3\text{O}_4$ @rGO decreased from ~93% in first cycle decreased to 69% in fifth cycles [33]. Moreover, MB degradation mechanisms, photodegradation pathways and toxicity of the intermediates were largely overlooked on these novel hybrid catalysts, which is essential to fundamentally understand the unique strength and potential limitations in dye wastewater treatment.

To develop a facile and scalable method for Fe_2O_3 @graphene with higher durability, this study presented a new synthesis method for the heterogeneous catalyst, $\alpha\text{-Fe}_2\text{O}_3$ anchored on graphene oxide nanosheets ($\alpha\text{-Fe}_2\text{O}_3$ @GO). The photodegradation of methylene blue (MB) was studied under ultraviolet light irradiation in presence of H_2O_2 . MB was chosen as a typical model cationic dye, as it represents a class of non-biodegradable dye and is widely used in the textile industry [47]. We also explored the effectiveness of decolorization and mineralization mechanisms of the MB dye and other typical dye or emerging contaminants (i.e., OII, OG, 2-NP, and E2) with $\alpha\text{-Fe}_2\text{O}_3$ @GO in a heterogeneous photo-Fenton process under different experimental variables such as pH, H_2O_2 levels, initial MB concentration, various organic structures, repeated use and scaling up experiments.

2. Experimental

2.1. Reagents and materials

MB with a molecular formula $\text{C}_{16}\text{H}_{18}\text{ClN}_3\text{S}\cdot\text{3H}_2\text{O}$, $\text{Fe}(\text{NO}_3)_3\cdot 9\text{H}_2\text{O}$ and H_2O_2 used in this study was purchased from Runjie Chemical Ltd. (Shanghai, China); Orange II (OII), Orange G (OG), rhodamine B (RhB), 2-nitrophenol (2-NP) and phenol, were all purchased from Sinopharm Chemical Reagent Ltd. (Shanghai, China). 17 β -estradiol (E2) was purchased from Eppendorf Company (Hamburg, Germany). Natural graphite was purchased from Guangfu fine chemical research institute (Tianjin, China), and used without further purification. Benzoquinone and methanol were purchased from Lingfeng Chemical Ltd. (Shanghai, China). Coumarin and tetraniromethane (TNM) were obtained from Aladdin Chemical Ltd. (Shanghai, China). All the other chemicals used were analytical grade. 2000 mg/L of MB stock solution was prepared by dissolving MB into deionized water and stored at room temperature. The working solutions were prepared by diluting MB stock solution with deionized water to desired concentrations.

2.2. Preparation and characterization of $\alpha\text{-Fe}_2\text{O}_3$ @GO catalyst

Graphene oxide (GO) was prepared from graphite powder by a modified Hummers method [48]. The $\alpha\text{-Fe}_2\text{O}_3$ @GO catalyst was prepared by gradually adding 0.1 g GO into 100 mL water and sonicated to obtain the GO dispersion. 4.04 g $\text{Fe}(\text{NO}_3)_3\cdot 9\text{H}_2\text{O}$ and 2.4 g urea was added slowly into above GO water solution. After 30 min sonication, the mixture underwent hydrolysis with magnetically stirred for 12 h in water-bath thermometer at 100 °C. After repeat separation by centrifugation and washing with deionized water, the obtained product was dried in vacuum oven at 60 °C and then manual powdered for further use.

The crystal structure of $\alpha\text{-Fe}_2\text{O}_3$ @GO was characterized by X-ray diffraction (XRD, Rigaku D/Max-2500, Japan) employing $\text{Cu K}\alpha$ as the source of radiation at $\lambda = 1.54056 \text{ \AA}$ over an angular range between 5° and 70°. Surface morphology was characterized by a field emission scanning electron microscope (FE-SEM, S-4800, Hitachi, Japan). High resolution transmission electron microscope (HRTEM) images were measured on HT7700 electron microscopy with resolution of 0.204 nm and the accelerating voltage of 120 kV.

The Fourier transform infrared (FT-IR) spectrum was recorded with a GX spectrophotometer (Perkin Elmer, USA) with the KBr wafer technique. The UV-vis diffuse reflectance spectra (UV-vis DRS) of α -Fe₂O₃ and α -Fe₂O₃@GO samples were obtained using a U-4100 spectrophotometer (Hitachi, Japan), with a BaSO₄ reference to determine the relationship between the spectroscopic properties and light adsorption efficiency. Photoluminescence (PL) emission spectra were measured using Fluorescence Spectrophotometer (F-4500, Hitachi, Japan) with an excitation wavelength of 254 nm at room temperature, and the emission spectra were collected between 265 and 500 nm. The excitation and emission slit were all set at 2.5 nm. The iron concentration of leaking was determined by Inductively Coupled Plasma-optical emission spectroscopy (ICP-OES, OPTIMA8000, PE, USA) with the detection limit of 0.030 mg/L. The surface elemental analysis of α -Fe₂O₃@GO before and after MB decolorization using X-ray photoelectron spectroscopy (XPS) was determined with an Axis Ultra spectrometer (Kratos, Japan). The binding energies (BE) were referenced to the C1s peak at 284.6 eV and fitted with XPSpeak41 software.

2.3. Experimental procedure

The photocatalytic degradation experiments were carried out in a cylindrical borosilicate evaporating dish with a diameter of 15 cm and a height of 7 cm. A 100 W high-pressure mercury lamp with a main wavelength of 365 nm (Phillips GGY100Z ballast) was located 21 cm above the centre of solution in the dish reactor to achieve the irradiation intensity of 1.4 mW/cm². Typically, catalytic degradation experiments were performed by adding 100 mg of α -Fe₂O₃@GO particles and H₂O₂ (1.10 mM) into 400 ml volume of 40 mg/L of MB solution in a borosilicate evaporating dish without adjusting pH. The pH was adjusted with 1 M HCl or 1 M NaOH. All the experiments were stirred with a magnetic stirrer at 20 °C. After different time intervals, the reaction suspension was withdrawn from the reactor and centrifuged (Kubota-3700, Kubota, Japan). The UV-vis absorbance of the supernatant was measured on a UV-vis spectrophotometer at 665 nm corresponding to the maximum absorbance of MB (UV-1102, Tianmei Tech comp Limt. Co., China). The percentage of MB decolorization was attained by:

$$\text{MB decolorization ratio} = \frac{(C_0 - C_t)}{C_0} \times 100\% \quad (1)$$

where C_0 and C_t represent the concentration of MB at initial and desired time intervals, separately. Sulphate and nitrate anions formation was detected by an ion chromatography system (ICS-2500, Thermo Fisher Scientific Inc., United States) and the degree of mineralization was monitored by the total organic carbon (TOC) (TOC-5050, Shimazdu, Japan) with standard deviation below 0.2 mg/L.

To assess the effects of initial pH, H₂O₂ dose, MB initial concentration, and organic structures on decolorization of MB, the same operation was performed except changing the concentrations of H₂O₂ or MB. To assess the organic structures on decolorization of MB in this treatment, 40 mg/L various organics (i.e., MB, RhB OII and OG) were used and they were detected by a UV-vis spectrophotometer (UV-1102, Tianmei Tech comp Limt. Co., China). 2-NP, E2 and phenol were detected by an ultra-pressure liquid chromatography (UPLC LC-20A, Shimadzu, Japan). To assess the stability and reusability of the catalyst, 10 consecutive cycles were conducted with 60 min in each cycle of the heterogeneous photo-Fenton reaction. Briefly, 100 mg of α -Fe₂O₃@GO and H₂O₂ (1.10 mM) were added into 400 ml of 40 mg/L of the MB solution without adjusting pH. Other procedures were the same as mentioned in Section 2.3. After each experiment, α -Fe₂O₃@GO was centrifuged and washed with DI water before the reuse in the next adsorption-photocatalytic reaction cycle.

Photodegradation intermediates of MB were detected by liquid chromatography coupled with tandem mass spectrometer (LC/MS/MS, Waters ACQUITY UPLC XEVO@TQD, USA). Waters ACQUITY UPLC® BEH HILIC (1.7 μ m, 2.1 mm × 100 mm) was employed in LC/MS/MS analysis. The binary solvent system was consisting of 1:1 (v/v) of 0.1% formic acid in water and acetonitrile. The MS source conditions were as follows: typical ESI-MS ion spray interface was operated in the MS scan mode between m/z 20–400; capillary voltage of 3.5 kV; cone voltage of 25 V; sheath gas (N₂) flow rate of 800 L/h; heated capillary temperature of 400 °C; source temperature of 150 °C.

Some degradation intermediates or by-products of MB may have increased toxicity and elevated environmental risks. Thus, it is necessary to test the biological toxicity of the reaction solution after photodegradation. Luminous bacteria (*Vibrio qinghaiensis*), as the common indicator of biological toxicity were used to evaluate the toxicity of MB. For the acute toxicity test, the luminescent bacterium Q67 (*Vibrio qinghaiensis*) in a freeze-dried powder form was reactivated in 5 mL recovery liquid (0.85% NaCl). The freshly prepared reactivated bacterial suspension (0.05 mL) was added to the 2 mL reaction solution. 0.05 mL bacteria solution mixed with 2 mL recovery liquid was used as the blank. After 15 min exposure of the bacteria to the sample at 20 °C, the relative luminosity of the bioluminescent bacterium was measured with luminescence at 490 nm by a BHP9514-Drinking water safety detector (Bingsong photonics technology Limt. Co., Beijing, China). The toxicity was indicated by the changes in relative luminosity:

$$\text{Relative luminosity} = \frac{E_t}{E_0} \times 100\% \quad (2)$$

where E_0 and E_t is the relative luminosity of Q67 exposed to the blank control and the samples at any time, respectively.

2.4. Measurement of radical formation

To unravel the mechanism involved in the catalytic degradation of MB in α -Fe₂O₃@GO + H₂O₂ + UV system, hydroxyl radical (\cdot OH) and superoxide radical ($O_2^{\cdot-}$) were measured as they are common radicals in Fenton systems in the presence of H₂O₂ [49]. Methanol (MeOH) and benzoquinone (BQ) were added to this catalytic system as obligate \cdot OH and $O_2^{\cdot-}$ scavengers [50], respectively. The radical formation was indicated by the concentration decline of these two scavengers. The quantitative generation of hydroxyl radicals was determined by a fluorescence technique using 1 mM of coumarin as a chemical probe and the TNM method was used to quantify the $O_2^{\cdot-}$ using the UV-vis spectrophotometer [51].

3. Results and discussion

3.1. Characterization of the catalyst

Fig. 1 shows the typical characteristic peaks of the synthesized α -Fe₂O₃@GO nanocomposite, GO, and graphite. For graphite, there was only one peak at $2\theta = 25.6^\circ$, which disappeared after being converted to GO. A distinguished peak at 2θ of 10.6° showed up for GO, indicative of the successful conversion from natural graphite to GO. The main diffraction peaks of α -Fe₂O₃@GO particles were indexed to the XRD pattern of pure orthorhombic phase α -Fe₂O₃ (JCPDS No. 33-0664), indicating the formation of highly crystalline hexagonal α -Fe₂O₃. No impurity peak was detected in the α -Fe₂O₃@GO nanocomposites during hydrolysis of ferric ions. However, no diffraction peaks of GO were detected in the α -Fe₂O₃@GO, probably because the intercalation of α -Fe₂O₃ nanoparticles in GO layers altered the crystalline structures of GO during the synthesis.

The morphology of the GO and α -Fe₂O₃@GO particles were revealed by SEM and TEM images. **Fig. 2a** presents a fibre-like

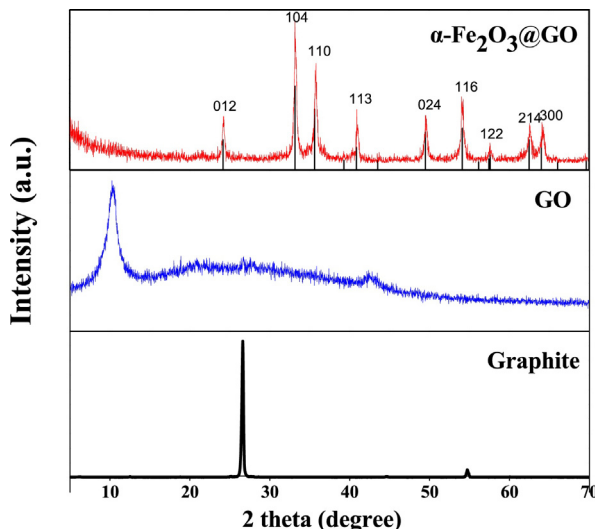


Fig. 1. XRD patterns of α -Fe₂O₃@GO, GO and natural graphite.

structure of GO with wrinkled edge and smooth surface, which corrugated together with sizes in the range of about several micrometre. The SEM image of α -Fe₂O₃@GO in Fig. 2b shows that a great quantity of irregular sphere-like particles of α -Fe₂O₃ was well dispersed on the surface of GO sheets at a high density. Similar distribution of the α -Fe₂O₃ nanoparticles on GO could be observed in the TEM image in Fig. 2c. From the SEM and TEM images, we randomly selected more than 20 single particles of α -Fe₂O₃ to statistically determine the average primary diameter of α -Fe₂O₃ nanoparticles to be 45 ± 10 nm. The iron content in α -Fe₂O₃@GO catalyst was approximately 49.6% as detected by ICP-OES.

The FTIR spectra in Fig. 3 show that GO had a broad band at 3424 cm^{-1} attributed to the OH stretching vibration of GO structural OH groups, which is in good agreement with previous work [52]. The characteristic band at 1642 cm^{-1} is due to the C=O stretching of carboxylic groups and the band at 1037 cm^{-1} corresponding to the C–O stretching vibrations of alkoxy group [53]. The typical functional groups of GO also could be observed in the FTIR of α -Fe₂O₃@GO in Fig. 3a, indicating an anchorage of α -Fe₂O₃ nanoparticles on GO. But the positions of the bonds were slightly red shifted and sharpness of the peaks were changed, which suggested the coordination environment of the functional groups in α -Fe₂O₃@GO may be changed due to the formation of Fe–O–C chemical bonds [54]. For example, the characteristic peak at 1642 cm^{-1} corresponding to C=O stretching vibration of –COOH in the GO shifts to 1600 cm^{-1} due to the complexity of –COO[–] with iron in α -Fe₂O₃ [55]. The FTIR spectrum of α -Fe₂O₃@GO particles exhibited an intensive band at 552 cm^{-1} ascribed to the Fe–O stretching vibrations in α -Fe₂O₃ [56]. Comparing the FTIR

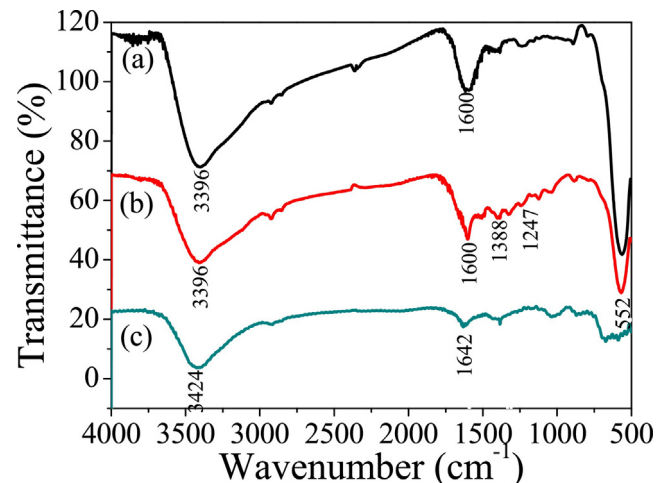


Fig. 3. FTIR absorption spectra of α -Fe₂O₃@GO before and after photodegradation and GO in a, b, and c lines respectively.

spectrum of α -Fe₂O₃@GO after MB photocatalytic degradation in Fig. 3b with that of pure α -Fe₂O₃@GO (Fig. 3a), the intensity of bands at 1388 cm^{-1} and 1247 cm^{-1} became stronger, which was attributed to the C–N (the bond between the side aromatic ring and the nitrogen atom) vibration and C–NH₃ (the bond between CH₃ and the nitrogen atom) stretching [57]. These bonds could result from the accumulation photo-degradation intermediates of MB on the surface of the catalyst. However, other functional groups of α -Fe₂O₃@GO after MB degradation remained almost identical with the original α -Fe₂O₃@GO, demonstrating that the excellent durability or stability of α -Fe₂O₃@GO.

According to the above results, the formation of α -Fe₂O₃ on the surface of GO could involve several steps: (1) the positive Fe³⁺ adsorbs on the sites of GO through electrostatic interaction due to abundance of negative oxygen-containing group of GO, such as hydroxyl, epoxy and carboxyl groups; (2) Urea slowly hydrolyzes and increase the solution pH that induces precipitation of Fe³⁺ on the active sites of GO; (3) Nucleation, crystal growth, and formation of α -Fe₂O₃ nanoparticle on the active sites of GO, as confirmed by formation Fe–O–C bonds through FTIR.

Fig. 4a shows that the UV-vis spectra of pure α -Fe₂O₃ had an absorption edge at approximately 630 nm ascribed to the intrinsic band gap of the α -Fe₂O₃ solid solution ($\sim 2.2\text{ eV}$) [58]. α -Fe₂O₃@GO exhibited a significant increase in light absorption and a slightly red-shift due to the narrowing of the band gap of α -Fe₂O₃@GO which could be due to the formation of the Fe–O–C bond between α -Fe₂O₃ and GO [58]. α -Fe₂O₃@GO greatly increases the light absorbance comparing with that of α -Fe₂O₃ due to the interaction with GO matrix. Photoluminescence (PL) spectra in Fig. 4b were recorded to examine the electronic interactions between

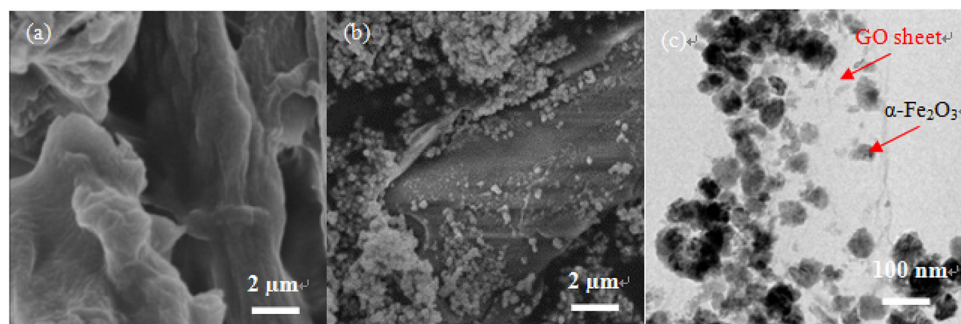


Fig. 2. SEM images of GO (a), α -Fe₂O₃@GO (b) and TEM image of α -Fe₂O₃@GO (c).

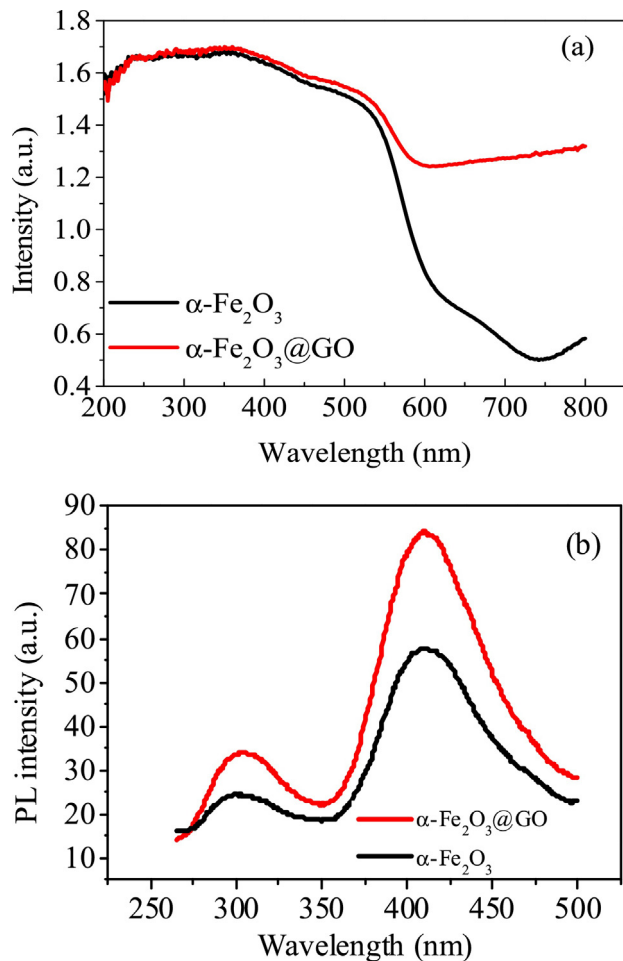


Fig. 4. UV-vis diffuses reflectance spectra (a) and PL spectra (b) of $\alpha\text{-Fe}_2\text{O}_3$ and $\alpha\text{-Fe}_2\text{O}_3\text{@GO}$.

$\alpha\text{-Fe}_2\text{O}_3$ and GO. The observed PL strengthening effect of $\alpha\text{-Fe}_2\text{O}_3\text{@GO}$ reveals a strong interaction between the excited state of $\alpha\text{-Fe}_2\text{O}_3$ and GO, which was probably associated with photo-induced electrons transfer to $\alpha\text{-Fe}_2\text{O}_3$ because the potential of GO is far more negative than that of conductive band of $\alpha\text{-Fe}_2\text{O}_3$. This phenomenon occurred because the photo-induced carriers rapidly transfer from GO to $\alpha\text{-Fe}_2\text{O}_3$. This result facilitated the efficient recycling of Fe(III)–Fe(II) pairs on the surface of $\alpha\text{-Fe}_2\text{O}_3\text{@GO}$ thus enhance the photocatalytic degradation efficiency [59].

3.2. Photo-Fenton catalytic activity of $\alpha\text{-Fe}_2\text{O}_3\text{@GO}$

The decolorization kinetics of MB under different conditions is shown in Fig. 5a. The decolorization rate of MB by $\alpha\text{-Fe}_2\text{O}_3\text{@GO}$ in the dark gradually increased and reached a plateau at 34% (see black square data). With UV photolysis alone, the equilibrium was reached about 29%. The decolorization of MB by $\alpha\text{-Fe}_2\text{O}_3\text{@GO} + \text{UV}$ improved slightly (see red dot data) to 42.4% owing to the catalytic properties of $\alpha\text{-Fe}_2\text{O}_3\text{@GO}$ and the produced $\cdot\text{OH}$ [60]. With H_2O_2 and UV irradiation, the decolorization rate of MB reached to 94.7% (see pink triangle data), which was attributed to the oxidation of chromophore in MB molecule by $\cdot\text{OH}$ generated from photolytic decomposition of H_2O_2 under UV irradiation [61]. Similar decolorization rates were achieved in $\text{TiO}_2 + \text{UV}$, $\alpha\text{-Fe}_2\text{O}_3 + \text{H}_2\text{O}_2 + \text{UV}$, and $\alpha\text{-Fe}_2\text{O}_3/\text{GO} + \text{H}_2\text{O}_2 + \text{UV}$. It is worth noting that the decolorization rate was highest for $\alpha\text{-Fe}_2\text{O}_3\text{@GO} + \text{H}_2\text{O}_2 + \text{UV}$ within the initial 40 min (e.g., the MB decolorization ratio of 64.6% was

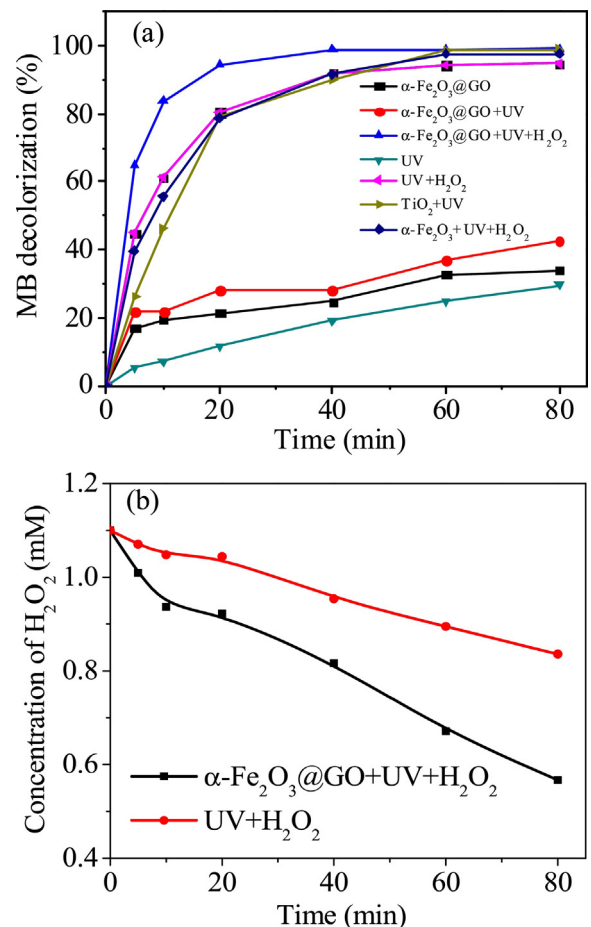


Fig. 5. The decolorization of MB under different conditions (a) and concentration of H_2O_2 varied in different heterogeneous Fenton processes (b) with time.

already reached within first 5 min, followed by $\text{UV} + \text{H}_2\text{O}_2$ and $\alpha\text{-Fe}_2\text{O}_3 + \text{H}_2\text{O}_2 + \text{UV}$.

Despite of a relatively high decolorization of MB in $\text{H}_2\text{O}_2 + \text{UV}$ system, the decomposition rate of H_2O_2 (Fig. 5b) in $\text{H}_2\text{O}_2 + \text{UV}$ system was 24.0% within 80 min, much lower than that in $\alpha\text{-Fe}_2\text{O}_3\text{@GO} + \text{H}_2\text{O}_2 + \text{UV}$ of 48.4%. Clearly, the $\alpha\text{-Fe}_2\text{O}_3\text{@GO}$ catalyst could promote the activation and decomposition of H_2O_2 owing to its high surface area and a large number of catalytic active sites that enables H_2O_2 to have full access to the $\alpha\text{-Fe}_2\text{O}_3$ catalyst and efficient electron transfer.

The kinetics of MB decolorization by $\alpha\text{-Fe}_2\text{O}_3\text{@GO}$ in photo-Fenton system is shown in Fig. 5a (blue line), which has two stages: the first stage (0–20 min) is likely controlled by available Fe^{2+} on the surface of the catalyst and the concentration of H_2O_2 , and the second stage (20–60 min) had a slow degradation process due to the accumulation of intermediates of MB and consummation of H_2O_2 . To compare the MB degradation reaction kinetics, the experimental data were fitted with the pseudo-first-order and pseudo-second-order kinetic model [33]:

$$\ln \left(\frac{C_t}{C_0} \right) = -k_1 \times t \quad (3)$$

$$\frac{1}{(C_t - C_e)} = \frac{1}{(C_0 - C_e)} + k_2 \times t \quad (4)$$

where C_t is the MB concentration at time, t , C_0 is the initial MB concentration at $t=0$ and C_e is the equilibrium MB concentration. k_1 is the apparent first-order kinetic rate constants. K_2 is the apparent second-order kinetic rate constant. The kinetics of MB decolorization by $\alpha\text{-Fe}_2\text{O}_3\text{@GO}$ in photo-Fenton system

Table 1

First-order and second-order kinetic constants of MB decolorization under different experimental conditions.

Reaction type	First-order kinetic rate constant (min ⁻¹)	R ²	Second-order kinetic rate constant (L/mg/s)	R ²
UV	0.0048	0.957	0.0001	0.991
H ₂ O ₂ + UV	0.0467	0.990	0.0073	0.992
α-Fe ₂ O ₃ + UV + H ₂ O ₂	0.0827	0.992	0.0160	0.842
α-Fe ₂ O ₃ @GO + UV	0.0190	0.943	0.0002	0.765
α-Fe ₂ O ₃ @GO adsorption	0.0040	0.952	0.0002	0.818
α-Fe ₂ O ₃ @GO + UV + H ₂ O ₂	0.1953	0.997	0.0414	0.916
TiO ₂ + UV	0.0669	0.994	0.0251	0.744

was fitted with Eqs. (3) and (4). Table 1 shows the results of K_1 and the corresponding R^2 that indicate the data fitting using the pseudo-first-order kinetics model is reasonable. Similarly, the pseudo second-order kinetic rate constant for α-Fe₂O₃@GO was 0.0414 mg⁻¹ L s⁻¹ with a R^2 value of 0.916. Comparing R^2 , it seems that pseudo first-order kinetics model is more applicable for explaining the decolorization of MB in α-Fe₂O₃@GO + H₂O₂ + UV system. Clearly, the α-Fe₂O₃@GO + H₂O₂ + UV system had the highest reaction rate constant than any other combinations (i.e. 4.2-fold that of H₂O₂ + UV system, 2.9-fold that of the classical Degussa P25 TiO₂ + UV and 2.4-fold that of α-Fe₂O₃ + H₂O₂ + UV), indicating that the introduction of GO greatly enhanced the catalytic performance of α-Fe₂O₃.

3.3. Influence of environmental factors on MB decolorization

3.3.1. Effect of pH

The catalytic decolorization of MB in the α-Fe₂O₃@GO + H₂O₂ + UV was evaluated at different initial pH from 3 to 12. The results in Fig. 6a show that the catalytic activity of the α-Fe₂O₃@GO catalyst remained almost the same in the pH range of 3–12 with a high decolorization ratio of 99% within 80 min reaction. The wide working pH could be attributed to the electronegativity surface of GO that favours the adsorption of cationic MB through π–π stacking and electrostatic interaction [32]. Furthermore, the solution pH decreased with an increase in irradiation time, resulting from the formation of acidic intermediates or final inorganic acids [21]. Yang et al. reported MB decolorization by Fe–Fe₃O₄@rGO in Fenton system with the optimum operation pH of 3. With pH decreasing to 2 or increasing to 4, the decolorization ratio of MB sharply decreased from ~96% to 87% or 53% [33]. Hence, heterogeneous photo-Fenton process α-Fe₂O₃@GO + H₂O₂ + UV can be effectively used in a wide pH range without acidification, which is superior over the conventional Fenton-like reactions.

3.3.2. The effect of initial MB concentrations

Fig. 6b compared the catalytic performance in various initial concentrations (i.e., 40, 80 and 100 mg/L of MB) and the results show that the decolorization of MB slowed down with the increase of the initial concentration of MB solution. At high concentrations, the MB adsorption onto catalyst surface may reach saturation rapidly and slow down photocatalytic degradation [62], probably because electron transfer to the catalyst surface was intervened by adsorbed MB. Furthermore, MB and its intermediates could compete with each other for limited reactive sites on the catalyst surface, hence inhibiting the overall degradation of MB [63].

3.3.3. Effect of H₂O₂ concentration

Fig. 6c shows the effect of the H₂O₂ concentrations on decolorization of MB in α-Fe₂O₃@GO + H₂O₂ + UV system. The decolorization of MB increased obviously with the increase of the molar concentration of H₂O₂ from 0.55 to 1.10 mM, because of the boost of •OH generated by H₂O₂ under UV. However, when H₂O₂ increased from 1.10 to 4.40 mM, the increase of decolorization efficiency became less significant, because of the so-called scavenging

effect of excessive H₂O₂, in which H₂O₂ + •OH → H₂O + HO₂• may occur and thus reduce the availability of •OH and degradation efficiency. Hydroperoxyl radicals (HO₂•) generated are substantially less reactive and do not contribute to the oxidation of organic dyes [64]. Therefore, to avoid the excessive of H₂O₂ and potential depression on degradation efficiency, a proper dose of H₂O₂ is required.

3.3.4. The effectiveness in degradation of various structural organics

Fig. 6d shows the adsorption and degradation rates of various model organic pollutants in α-Fe₂O₃@GO + H₂O₂ + UV system. Three types of organic compounds were selected based on their distinct surface charges, including cationic dyes (methylene blue, MB and rhodamine B, RhB), anionic dyes (Orange II, OII and Orange G, OG), neutral compounds (phenol and 2-nitrophenol, 2-NP) and endocrine disruptor (17β-estradiol, E2). The adsorption rate was in the order of MB ≈ RhB > OII > 2-NP > OG > E2 > phenol. The pseudo-first order kinetic rate constants were in the order of MB (0.1953 min⁻¹, R^2 = 0.996) ≈ RhB (0.1944 min⁻¹, R^2 = 0.900) > phenol (0.1231 min⁻¹, R^2 = 0.992) ≈ E2 (0.1042, R^2 = 0.986) > OG (0.0638, R^2 = 0.960) ≈ OII (0.060 min⁻¹, R^2 = 0.972) ≈ 2-NP (0.0608 min⁻¹, R^2 = 0.995).

α-Fe₂O₃@GO showed both high adsorption and degradation rates to cationic compounds of MB and RhB probably due to the strong electrostatic interaction between negatively charged graphene oxide surface and cationic dyes. By contrast, α-Fe₂O₃@GO showed moderate adsorption rates for OII and OG (around 15%) due to the strong electrostatic repulsion between negatively charged graphene oxide supports with anionic compounds. The photocatalytic degradation rates were as high as those of MB and RhB (near 96% after 80 min irradiation). Although the adsorption of phenol, 2-NP and E2 on the surface of α-Fe₂O₃@GO were relatively low and below 13% after 20 min in the dark, the degradation rates of phenol and E2 were excellent (over 99% after 60 or 80 min irradiation). This result shows that α-Fe₂O₃@GO can highly and effectively facilitate the photocatalytic degradation of a broad spectrum of organic pollutants, which is compared for the first time. Many reported studies showed the photo-Fenton catalysts often work effectively towards specific groups of charged dyes. For example, BiOBr showed higher activity towards RhB than that of MB [65]. Mesoporous TiO₂ degrades MB faster than OII [66]. Thus, the incorporation of GO with α-Fe₂O₃ has led to high efficient photocatalytic degradation of a wider range of both charged and neutral organic pollutants.

3.3.5. Stability and reusability of α-Fe₂O₃@GO

Fig. 6e shows that the MB decolorization ratio remained at a level of near 99% after 10 consecutive cycles of repeated use, highlighting its excellent stability and photoactivity. As seen in FTIR results, no essential chemical and structural changes occurred to the catalyst after repeated uses. More importantly, irons leaching from the catalyst were not detected or lower than the detection limit of ICP-OES.

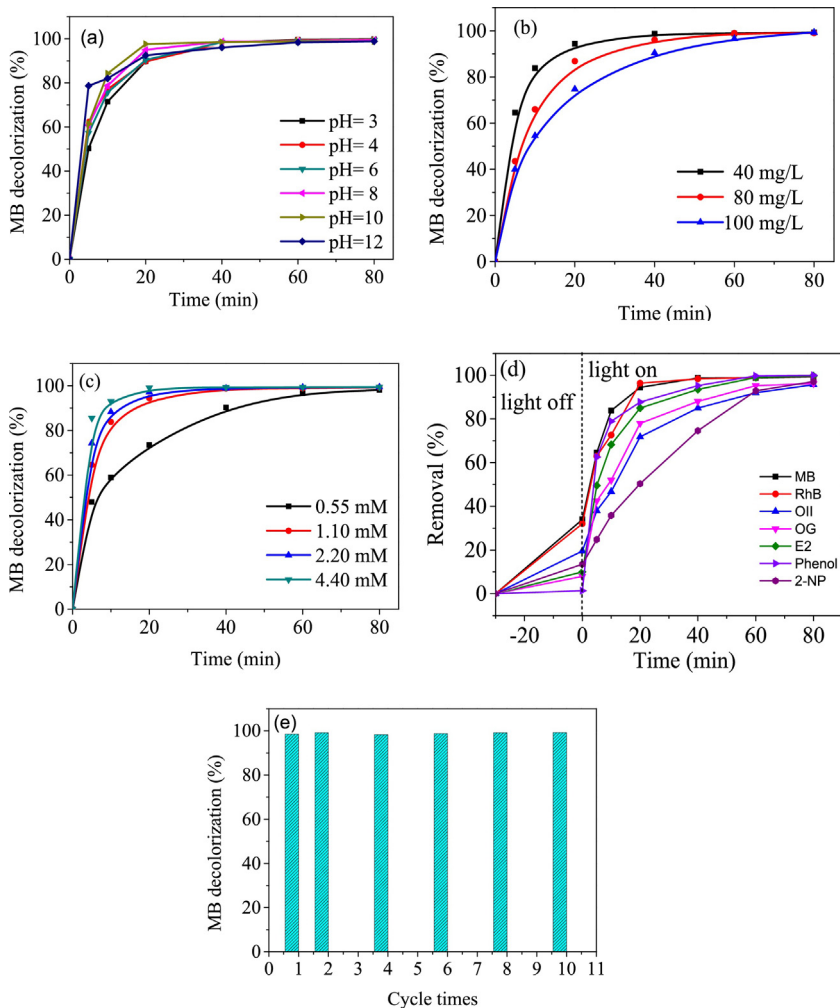


Fig. 6. Influence of initial solution pH value (inset of first-order kinetic constants) (a), influence of initial concentration (b), influence of H₂O₂ concentrations (c) on MB decolorization, effectiveness in degradation various organics (d) and durability of catalyst after 10-fold adsorption-degradation cycles (e) in the α -Fe₂O₃@GO + H₂O₂ + UV system.

3.4. Photocatalytic degradation mechanisms

3.4.1. The evolved UV-vis spectral during MB decolorization

To analyze the decolorization mechanisms, the temporal evolution of the UV-vis spectra of the reaction solution was investigated. As shown in Fig. 7, two main absorbance peaks of the MB spectra were observed. In the ultraviolet region, the peaks at 291 nm was ascribed to the $\pi \rightarrow \pi^*$ transition related to unsaturated conjugate aromatic rings [20]. In the visible range, the absorption peak at 665 nm was attributed to the chromophores functional groups of MB and its dimers, namely $-C=S$ and $-C=N$, which may undergo hemolytic cleavage [63]. The intensity of the signals at 291 and 665 nm dramatically decreased and finally disappeared with reaction time. The quick decay of the peak at 665 nm was the decolorization evidence for the destruction of the conjugate structure in MB molecules. The disappearance of absorbance at 291 nm indicated the aromatic fragments of MB and its intermediates were degraded. Notably, the position of the maximum absorbance peak at the same wavelength of 665 nm was still there without shift with reaction time. However, Wen et al. reported a marked blue-shift of UV-vis absorbance for MB solution in the MnO₂ or MnO₂/heating systems [67]. In the sole MnO₂ system, the UV-vis absorbance peak of MB shifted from 665 nm (max for MB) to 650 nm (maximum absorption wavelength for Azure B) at a reaction time of 5 min and then shifted to 600 nm (maximum

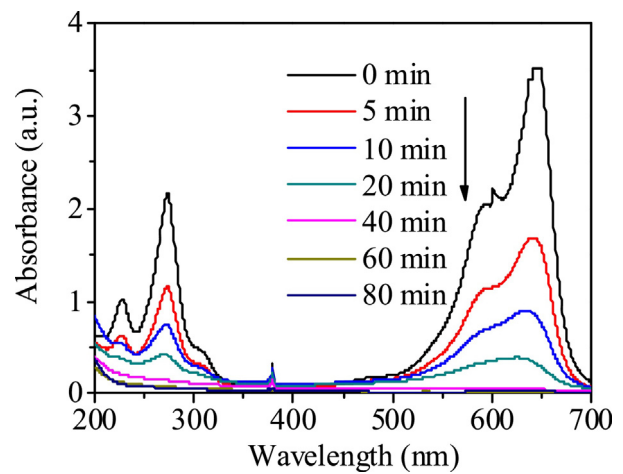


Fig. 7. Temporal evolution of the UV-vis spectra during decolorization of MB in the α -Fe₂O₃@GO + H₂O₂ + UV system.

absorption for Thionin) at 24 h reaction time. In MnO₂/heating system, two distinguished peaks at 640 nm (max for Azure A) to 618 nm (max for Azure C) were observed at 5 min. N-demethylation of MB containing auxochromic methylamine groups is important for catalytic degradation in their study. Zhang et al. also indicated

that, the peak 665 nm of MB blue shifted by as much as 20 nm in the TiO_2 system, which showed the occurring of N-demethylation intermediates of MB [6]. Compared with these literatures, the initial step of MB degradation in the degradation in our catalytic reaction may not involve N-demethylation, which will be further discussed below in the degradation pathway analysis.

3.4.2. Mineralization and dominating ROS

In addition to decolorization, the extent of MB mineralization is also important for practical industrial applications. To quantify the mineralization of MB in the reaction, TOC in the MB solution as a function of time was measured and shown in Fig. 8a. The TOC removal almost linearly increased with time until reaching 56%, implying a rapid and complete decomposition of MB at the initial 80 min. In accordance with decolorization of MB in Fig. 6d after 10 cycles, the TOC removal ratio remained almost above 50% after 10 cycles of photodegradation. About 44% of TOC left in the solution due to the accumulation of intermediates such as carboxyl acids [68]. In this study, complete TOC removal could be achieved by prolonging reaction time or constantly maintaining high level H_2O_2 after breaking down the chromophore group of dye molecule [14]. Yuan et al. reported that in the $\text{Si-Al}/\alpha\text{-FeOOH}/\text{H}_2\text{O}_2$ catalytic oxidation system, almost 100% of TOC removal was obtained after further adding 1 mL H_2O_2 to the reaction solution [69]. Since the total mineralization of an organic compound containing C, S and N functional groups in MB results in the formation of carbon dioxide (or carbonate ions), sulfate, nitrate and/or ammonium compounds, inorganic ions (SO_4^{2-} and NO_3^-) in solution were tested by ion chromatogram to confirm the presence of complete mineralization. Fig. 8a also shows that SO_4^{2-} was produced at the initial stage of the reaction due to the oxidation of the sulfonyl group in MB molecules. Generally speaking, sulfur in a S^+ –aromatic bond in MB is not easy to be oxidized because of its +4 valence state [70]. The adsorption through positive S-containing group on the surface of negative charged $\alpha\text{-Fe}_2\text{O}_3@\text{GO}$ may facilitate the oxidation and formation of sulfate anions in this heterogeneous system. By contrast, the concentration of NO_3^- stayed at a constant low level during the whole process, indicative of a limited N-demethylation. The substantial amount N-containing species therefore remained on the catalyst surface or present in the solution, which was confirmed by our FTIR result.

Fig. 8b shows the difference in the degradation of MB with or without the addition of the scavenger, BQ, indicating that $\text{O}_2^\bullet-$ was involved in MB degradation. By contrast, a severe inhibitory effect on the degradation reaction of MB was found after the addition of MeOH that severely quenched the produced $\bullet\text{OH}$ species. Thus, $\bullet\text{OH}$ species are dominant responsible radicals in this heterogeneous Fenton reaction. Fig. 8c shows the formation concentration of $\text{O}_2^\bullet-$ reached a maximum of 1.28 mM at 20 min. After adding $\text{O}_2^\bullet-$ quencher, BQ, the MB decolorization was slightly affected. The maximum concentration of $\bullet\text{OH}$ reached 0.36 mM after 80 min. After quenching $\bullet\text{OH}$ with MeOH, the MB decolorization was greatly inhibited. Clearly, the oxidation potential of $\text{O}_2^\bullet-$ could be limited towards MB even though the formation concentration of $\text{O}_2^\bullet-$ was much higher than that of $\bullet\text{OH}$. The quantitative analysis of $\text{O}_2^\bullet-$ and $\bullet\text{OH}$ was consistent with MB decolorization results by using corresponding radical quenchers in Fig. 8b.

3.4.3. Photocatalytic degradation pathway of MB

In Fig. S1 in the electronic supporting information (ESI), the mass spectra show the detected hydroxylated intermediates by LC/MS/MS, implying that hydroxylation could be a main mechanism for the degradation of MB via $\alpha\text{-Fe}_2\text{O}_3@\text{GO} + \text{H}_2\text{O}_2 + \text{UV}$ system. Previous work has demonstrated that the benzene ring of MB can be hydroxylated [71] and the $\text{C}-\text{S}^+-\text{C}$ could be converted to sulfone [72], which could justify the observations of intense

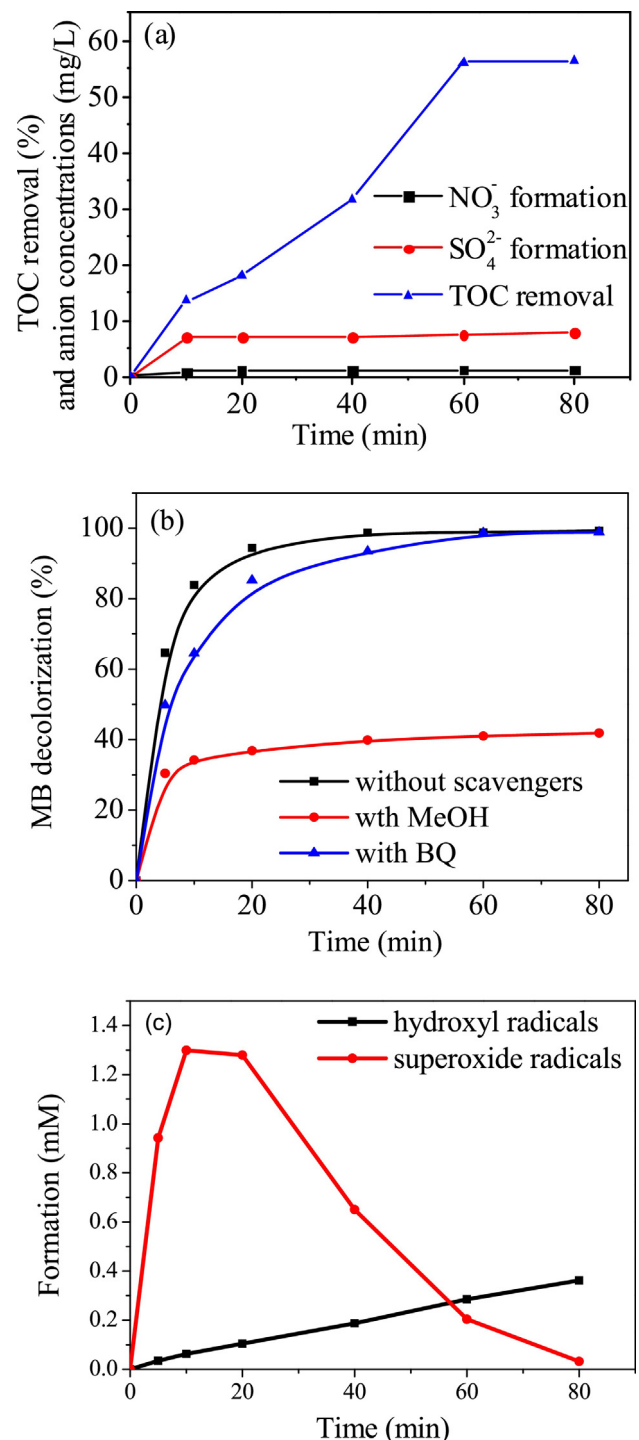


Fig. 8. TOC removal and the concentration evolution of SO_4^{2-} and NO_3^- (a), influences of radical scavengers on decolorization of MB (b), and concentration variations of $\text{O}_2^\bullet-$ and $\bullet\text{OH}$ with time (c) in the $\alpha\text{-Fe}_2\text{O}_3@\text{GO} + \text{H}_2\text{O}_2 + \text{UV}$ system.

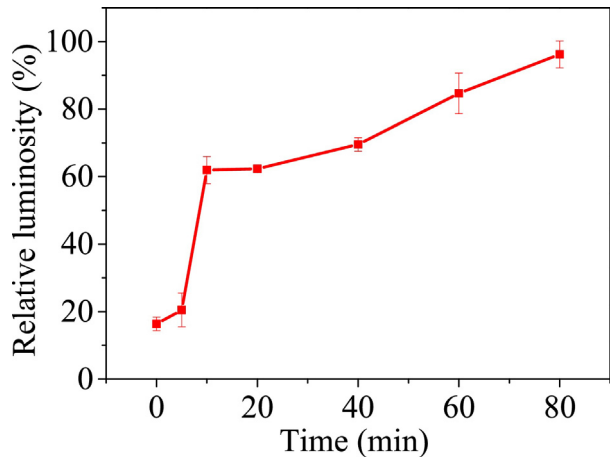
fragments corresponding to $m/z = 301, 326, 349, 365, 381$ and 396. Other hydroxylation on methyl group connected with nitrogen-atoms on the side ring could be attacked by $\bullet\text{OH}$, leading to the formation of fragments corresponding to $m/z = 326$. Large amounts of SO_4^{2-} anions present in the degradation of MB in the first 5 min (Fig. 8b) also suggest that the sulfone formed in MB molecules corresponds to the observed fragment at $m/z = 264$. The disruption of $\text{C}-\text{S}^+-\text{C}$ weakened the ring structure and thus led to the opening of the central aromatic ring. With the $\text{C}-\text{N}^+=\text{C}$ functional groups destroyed, $-\text{N}-(\text{CH}_3)_2$ groups were also degraded by successive

Table 2Binding energy and atomic surface concentration of detected elements for α -Fe₂O₃@GO.

Binding energy (eV)							
	Fe		O 1s				C 1s
	2p3/2	2p1/2		528.1	529.7	531.1	
Before	711.1	724.6	ND	528.1	529.7	531.1	ND
After	711.0	724.5	ND	ND	529.8	531.2	532.7

Atomic surface concentration (%)							
	Fe		O				C
	Fe ²⁺	Fe ³⁺		Fe–O _{oxides}	Fe–OH _{lattice}	Fe–OH _{ads} /C–O–Fe	
Before	14.30	76.1%	37.32	27.9%	63.6%	0	48.38
After	17.80	72.2%	23.9% 41.55 0	27.9% 50.0%	38.8%	11.2%	40.65

ND: no detection.

**Fig. 9.** Relative luminosity change with the reaction time in the α -Fe₂O₃@GO + H₂O₂ + UV system.

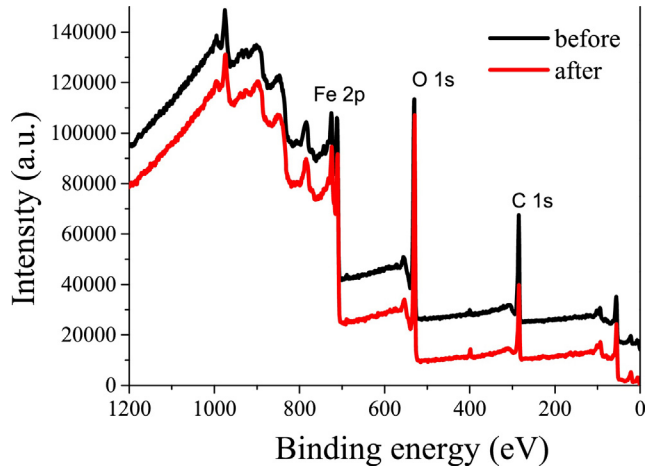
attacks of \bullet OH radicals, further inducing the breakup of the two side aromatic rings. Subsequent reactions produced charge-containing intermediates such as carboxylate (RCOO[–]) and R-NH₃⁺, which were further mineralized to carbon dioxide, water and inorganic anions (SO₄^{2–} NH₄⁺ and NO₃[–]). A plausible degradation pathway for MB via α -Fe₂O₃@GO + H₂O₂ + UV Fenton process is proposed in Fig. S2.

3.4.4. Toxicity evaluation of degradation intermediates of MB

The potential adverse effect of degradation by-products or intermediates was assessed by monitoring the luminosity change of MB at an initial concentration of 40 mg/L. The luminosity rate increased from about 16.4% to 96.2% after irradiation for 80 min, indicating a reduction of the acute toxicity of the MB solution as a result of mineralization [73]. The MB degradation in the heterogeneous photo-Fenton reaction of α -Fe₂O₃@GO did not produce second pollution. Besides, the scaling up experiment of MB decolorization in α -Fe₂O₃@GO photo-Fenton system was performed. Figs. S3 and S4 show that MB decolorization ratio slightly decreased before 60 min when scale up to 1.5- or 2-fold. After the reaction proceeded for 60 min the MB decolorization ratio reached the same efficiency, indicating that scaling up did not significantly affect the degradation performance (Fig. 9).

3.4.5. Photocatalytic mechanism of α -Fe₂O₃@GO

The surface chemical bonding and states of α -Fe₂O₃@GO were investigated using XPS. Fig. 10 shows the Fe 2p, O 1s and C 1s

**Fig. 10.** XPS survey of α -Fe₂O₃@GO before and after decolorization of MB in the α -Fe₂O₃@GO + H₂O₂ + UV system.

core-level XPS spectra of α -Fe₂O₃@GO. The binding energy (BE) of Fe 2p observed at 711.1 eV was the characteristic doublet Fe 2p of Fe₂O₃ [41] which involves different redox status of surface α -Fe₂O₃ [74]. The two peaks centred at 711.1 and 724.6 eV can be ascribed to the core levels of Fe 2p3/2 and Fe 2p1/2, respectively with splitting energy of 13.5 eV, suggesting the presence of the oxidation state of Fe³⁺ [32]. In addition, a satellite peak located at 717.1 eV further confirmed the existence of Fe³⁺ species on the surface of α -Fe₂O₃@GO. The change of the Fe²⁺/Fe³⁺ ratios before or after the photocatalytic reaction was probably resulted from the conversion and recycling of Fe²⁺/Fe³⁺ on the surface of the catalyst in this photo-Fenton reaction. Table 2 shows three possible surface O 1s signals. The new peak at 531.2 eV corresponds to the Fe–O–C bond, which confirms the strong interfacial interactions between graphene oxide and α -Fe₂O₃ due to form Fe–O–C bonds [75]. The peak at 532.7 eV was ascribed to C–OH/C–O–C, suggesting that α -Fe₂O₃@GO would highly interact with MB or its intermediates through with oxygen-containing groups of GO to facilitate the enrichment of MB or its intermediates on the surface of the catalysts. The disappearing peak at 528.1 eV and decrease at the peak at 531.1 eV indicate that the surface hydroxyl may be involved in this photocatalytic reaction to form Fe–OH_{lattice}.

In summary, the degradation of MB should firstly begin with surface adsorption of MB onto α -Fe₂O₃@GO through electrostatic interaction and π – π stacking. Then, the decolorization could be initiated by the \bullet OH and O₂^{•–} radicals produced in photo-Fenton reaction catalyzed by α -Fe₂O₃@GO. Fe(III) on the surface of

α -Fe₂O₃@GO could be photo-reduced into Fe(II) or directly reduced by electrons. GO plays an important role in facilitating the photo-generated electrons transferring from the conduction band of α -Fe₂O₃ to surface Fe(III) of the catalysts [61]. For instance, the introduction of GO can speed up the redox recycling between Fe(II) and Fe(III) on the surface of α -Fe₂O₃@GO, which is the rate controlling step of the Fenton reaction. The formed Fe(II) in turn would accelerate the decomposition of H₂O₂ in solution and produce \cdot OH and Fe(III). Thus the enhanced decolorization and mineralization of MB would be observed through the oxidation by \cdot OH and O₂^{·-} radicals produced in α -Fe₂O₃@GO + H₂O₂ + UV system.

4. Conclusion

α -Fe₂O₃ impregnated graphene oxide (α -Fe₂O₃@GO) nanocomposites were synthesized and characterized. The heterogeneous Fenton catalyst α -Fe₂O₃@GO operated at a wider pH range (from 3 to 12) and exhibited faster decolorization ratio of MB than those of other combinations such as Degussa P25 TiO₂ + UV and α -Fe₂O₃ + H₂O₂ + UV. The catalyst was highly stable with consistently high decolorization and negligible iron leaching after 10 cycles of consecutive uses. Luminous bacteria toxicity evaluation showed that the toxicity of the MB solution was reduced with the reaction time of photocatalytic degradation without producing secondary pollutants. Hence, this photo-assisted Fenton process holds great promise in overcoming the identified challenges in conventional Fenton reaction. Also, the treatment process can be scaled up for practical application and achieve high efficient removal of a broad spectrum of various organic pollutants. The incorporation of GO with α -Fe₂O₃ nanoparticles greatly improved the catalytic efficiency and selectivity of α -Fe₂O₃ towards cationic organics and phenol like compounds.

Acknowledgements

This work is supported by China's NSF (No. 21377039) and the Shanghai international cooperation research projects (No. 14230710900).

Appendix A. Supplementary data

Supplementary data associated with this article can be found, in the online version, at <http://dx.doi.org/10.1016/j.apcatb.2017.01.075>.

References

- [1] T. Robinson, G. McMullan, R. Marchant, P. Nigam, *Bioresour. Technol.* 77 (2001) 247–255.
- [2] C.A. Martínez-Huitle, E. Brillas, *Appl. Catal. B: Environ.* 87 (2009) 105–145.
- [3] F.P. van der Zee, G. Lettinga, J.A. Field, *Chemosphere* 44 (2001) 1169–1176.
- [4] E. Brillas, C.A. Martínez-Huitle, *Appl. Catal. B: Environ.* 166–167 (2015) 603–643.
- [5] A.B. dos Santos, F.J. Cervantes, J.B. van Lier, *Bioresour. Technol.* 98 (2007) 2369–2385.
- [6] T.Y. Zhang, T. Oyama, S. Horikoshi, H. Hidaka, J.C. Zhao, N. Serpone, *Sol. Energy Mater. Sol. Cells* 73 (2002) 287–303.
- [7] S. Bae, D. Kim, W. Lee, *Appl. Catal. B: Environ.* 134–135 (2013) 93–102.
- [8] X. Yang, W. Chen, J. Huang, Y. Zhou, Y. Zhu, C. Li, *Sci. Rep.* 5 (2015) 10632.
- [9] M. Pariente, F. Martínez, J. Melero, J. Botas, T. Velegraki, N. Xekoukouloukis, D. Mantzavinos, *Appl. Catal. B: Environ.* 85 (2008) 24–32.
- [10] Y.P. Zhao, H.Y. Hu, *Appl. Catal. B: Environ.* 78 (2008) 250–258.
- [11] M. Munoz, Z.M. de Pedro, J.A. Casas, J.J. Rodriguez, *Appl. Catal. B: Environ.* 176 (2015) 249–265.
- [12] J. Bandara, J.A. Mielczarski, A. Lopez, J. Kiwi, *Appl. Catal. B: Environ.* 34 (2001) 321–333.
- [13] X.G. Wang, C.S. Liu, X.M. Li, F.B. Li, S.G. Zhou, *J. Hazard. Mater.* 153 (2008) 426–433.
- [14] J. He, W.H. Ma, J.J. He, J.C. Zhao, J.C. Yu, *Appl. Catal. B: Environ.* 39 (2002) 211–220.
- [15] G. Zhang, Q. Wang, W. Zhang, T. Li, Y. Yuan, P. Wang, *Photochem. Photobiol. Sci.* 15 (2016) 1046–1053.
- [16] Z.H. Xu, M. Zhang, J.Y. Wu, J.R. Liang, L.X. Zhou, B. Lu, *Water Sci. Technol.* 68 (2013) 2178–2185.
- [17] Z.H. Xu, Y.Q. Yu, D. Fang, J.Y. Xu, J.R. Liang, L.X. Zhou, *Ultrason. Sonochem.* 27 (2015) 287–295.
- [18] S.S. Chou, C.P. Huang, Y.H. Huang, *Environ. Sci. Technol.* 35 (2001) 1247–1251.
- [19] M. Hartmann, S. Kullmann, H. Keller, *J. Mater. Chem.* 20 (2010) 9002.
- [20] Y. Li, F.-S. Zhang, *Chem. Eng. J.* 158 (2010) 148–153.
- [21] J. Feng, X. Hu, P.L. Yue, *Environ. Sci. Technol.* 38 (2004) 5773–5778.
- [22] R. Matta, K. Hanna, S. Chiron, *Sci. Total Environ.* 385 (2007) 242–251.
- [23] Z. Tong, P. Zheng, B. Bai, H. Wang, Y. Suo, *Catalysts* 6 (2016) 58.
- [24] S. Ben Hammouda, F. Fourcade, A. Assadi, I. Soutrel, N. Adhoum, A. Amrane, L. Monser, *Appl. Catal. B: Environ.* 182 (2016) 47–58.
- [25] H. Bel Hadjtaief, P. Da Costa, P. Beaunier, M.E. Gálvez, M. Ben Zina, *Appl. Clay Sci.* 91–92 (2014) 46–54.
- [26] H. Gaffour, M. Mokhtari, *Res. Chem. Intermed.* 42 (2016) 6025–6038.
- [27] A. Özcan, A. Atilir Özcan, Y. Demirci, E. Şener, *Appl. Catal. B: Environ.* 200 (2017) 361–371.
- [28] S. Karthikeyan, M.P. Pachamuthu, M.A. Isaacs, S. Kumar, A.F. Lee, G. Sekaran, *Appl. Catal. B: Environ.* 199 (2016) 323–330.
- [29] Y. Fu, Q. Wei, B. Lu, X. Wang, S. Sun, *J. Alloys Compd.* 684 (2016) 419–427.
- [30] S. Stankovich, R.D. Piner, S.T. Nguyen, R.S. Ruoff, *Carbon* 44 (2006) 3342–3347.
- [31] S. Stankovich, D.A. Dikin, G.H. Domke, M.K. Kohlhaas, E.J. Zimney, E.A. Stach, R.D. Piner, S.T. Nguyen, R.S. Ruoff, *Nature* 442 (2006) 282–286.
- [32] F. Liu, S. Chung, G. Oh, T.S. Seo, *ACS Appl. Mater. Interfaces* 4 (2012) 922–927.
- [33] B. Yang, Z. Tian, L. Zhang, Y. Guo, S. Yan, *J. Water Process Eng.* 5 (2015) 101–111.
- [34] A. Muthukrishnaraj, S. Vadivel, V.P. Kamalakannan, N. Balasubramanian, *Mater. Res. Innov.* 19 (2015) 258–264.
- [35] Z. He, G. Gui, J. Liu, C. Guo, J.S. Loo, C.M. Li, T.T. Tan, *Nanoscale* 3 (2011) 4613–4616.
- [36] Y. Sun, X. Hu, W. Luo, H. Xu, C. Hu, Y. Huang, *ACS Appl. Mater. Interfaces* 5 (2013) 10145–10150.
- [37] D.-W. Jung, J.-H. Jeong, E.-S. Oh, *J. Alloys Compd.* 690 (2017) 42–50.
- [38] M. Aadil, W. Shaheen, M.F. Warsi, M. Shahid, M.A. Khan, Z. Ali, S. Haider, I. Shakir, *J. Alloys Compd.* 689 (2016) 648–654.
- [39] Z. Song, W. Liu, W. Wei, C. Quan, N. Sun, Q. Zhou, G. Liu, X. Wen, *J. Alloys Compd.* 685 (2016) 355–363.
- [40] S. Lee, J. Oh, D. Kim, Y. Piao, *Talanta* 160 (2016) 528–536.
- [41] Z. Xu, W. Li, Y. Zhang, Z. Xue, X. Guo, G. Zhang, *Ind. Eng. Chem. Res.* 55 (2016) 10591–10599.
- [42] G. Zan, Q. Wu, *Adv. Mater.* 28 (2016) 2099–2147.
- [43] B.C. Qiu, M.Y. Xing, J.L. Zhang, *J. Mater. Chem. A* 3 (2015) 12820–12827.
- [44] M. Zhang, B. Qu, D. Lei, Y. Chen, X. Yu, L. Chen, Q. Li, Y. Wang, T. Wang, *J. Mater. Chem.* 22 (2012) 3868.
- [45] G. Wang, T. Liu, Y. Luo, Y. Zhao, Z. Ren, J. Bai, H. Wang, *J. Alloys Compd.* 509 (2011) L216–L220.
- [46] X.J. Zhu, Y.W. Zhu, S. Murali, M.D. Stollers, R.S. Ruoff, *ACS Nano* 5 (2011) 3333–3338.
- [47] V.K. Gupta, R. Kumar, A. Nayak, T.A. Saleh, M.A. Barakat, *Adv. Colloid Interface Sci.* 193 (2013) 24–34.
- [48] W.S. Hummers Jr., R.E. Offeman, *J. Am. Chem. Soc.* 80 (1958) 1339–1339.
- [49] B.A. Smith, A.L. Teel, R.J. Watts, *Environ. Sci. Technol.* 38 (2004) 5465–5469.
- [50] Y. Lin, D. Li, J. Hu, G. Xiao, J. Wang, W. Li, X. Fu, *J. Phys. Chem. C* 116 (2012) 5764–5772.
- [51] D.-h. Kim, A.D. Bokare, M.S. Koo, W. Choi, *Environ. Sci. Technol.* 49 (2015) 3506–3513.
- [52] J.I. Paredes, S. Villar-Rodil, A. Martinez-Alonso, J.M.D. Tascon, *Langmuir* 24 (2008) 10560–10564.
- [53] J.F. Shen, Y.Z. Hu, M. Shi, N. Li, H.W. Ma, M.X. Ye, *J. Phys. Chem. C* 114 (2010) 1498–1503.
- [54] T.N. Narayanan, Z. Liu, P.R. Lakshmy, W. Gao, Y. Nagaoka, D. Sakthi Kumar, J. Lou, R. Vajtai, P.M. Ajayan, *Carbon* 50 (2012) 1338–1345.
- [55] X. Yang, X. Zhang, Y. Ma, Y. Huang, Y. Wang, Y. Chen, *J. Mater. Chem.* 19 (2009) 2710.
- [56] M. Das, D. Mishra, T.K. Maiti, A. Basak, P. Pramanik, *Nanotechnology* 19 (2008) 415101.
- [57] Z.Q. Yu, S.S.C. Chuang, *J. Phys. Chem. C* 111 (2007) 13813–13820.
- [58] Y. Hou, F. Zuo, A. Dagg, P. Feng, *Nano Lett.* 12 (2012) 6464–6473.
- [59] J. Yu, B. Yang, B. Cheng, *Nanoscale* 4 (2012) 2670–2677.
- [60] J.J. Pignatello, *Environ. Sci. Technol.* 26 (1992) 944–951.
- [61] J. Feng, X.J. Hu, P.L. Yue, *Environ. Sci. Technol.* 38 (2004) 269–275.
- [62] H.B. Hadjitaief, P. Da Costa, M.E. Galvez, M. Ben Zina, *Ind. Eng. Chem. Res.* 52 (2013) 16656–16665.
- [63] B. Zhou, X. Zhao, H.J. Liu, J.H. Qu, C.P. Huang, *Appl. Catal. B: Environ.* 99 (2010) 214–221.
- [64] M. Neamtu, C. Catrinescu, A. Kettrup, *Appl. Catal. B: Environ.* 51 (2004) 149–157.
- [65] D. Zhang, J. Li, Q. Wang, Q. Wu, *J. Mater. Chem. A* 1 (2013) 8622.
- [66] L. Kuang, Y. Zhao, L. Liu, *J. Environ. Monit.* 13 (2011) 2496–2501.
- [67] W.H. Kuan, C.Y. Chen, C.Y. Hu, Y.M. Tzou, *Int. J. Photoenergy* (2013) 9.
- [68] J.H. Ramirez, C.A. Costa, L.M. Madeira, *Catal. Today* 107–08 (2005) 68–76.
- [69] B.L. Yuan, J.G. Xu, X.T. Li, M.L. Fu, *Chem. Eng. J.* 226 (2013) 181–188.
- [70] H. Lachheb, E. Puzenat, A. Houas, M. Ksibi, E. Elaloui, C. Guillard, J.M. Herrmann, *Appl. Catal. B: Environ.* 39 (2002) 75–90.

[71] L.C.A. Oliveira, M. Goncalves, M.C. Guerreiro, T.C. Ramalho, J.D. Fabris, M.C. Pereira, K. Sapag, *Appl. Catal. A: Gen.* 316 (2007) 117–124.

[72] A. Houas, H. Lachheb, M. Ksibi, E. Elaloui, C. Guillard, J.M. Herrmann, *Appl. Catal. B: Environ.* 31 (2001) 145–157.

[73] H. Chaabane, E. Vulliet, F. Joux, F. Lantoine, P. Conan, J.F. Cooper, C.M. Coste, *Water Res.* 41 (2007) 1781–1789.

[74] X.M. Zhou, H.C. Yang, C.X. Wang, X.B. Mao, Y.S. Wang, Y.L. Yang, G. Liu, *J. Phys. Chem. C* 114 (2010) 17051–17061.

[75] P.H. Shao, J.Y. Tian, B.R. Liu, W.X. Shi, S.S. Gao, Y.L. Song, M. Ling, F.Y. Cui, *Nanoscale* 7 (2015) 14254–14263.